Stability of a radially stretching disk beneath a uniformly rotating fluid

M. R. Turner
Department of Mathematics, University of Surrey, Guildford, Surrey GU2 7XH, United Kingdom

Patrick Weidman
Department of Mechanical Engineering, University of Colorado, Boulder, Colorado 80309-0427, USA

(Received 1 March 2017; published 13 July 2017)

The steady radial stretching of a disk beneath a rigidly rotating flow with constant angular velocity is considered. The steady base flow is determined numerically for both a stretching and a shrinking disk. The convective instability properties of the flow are examined using temporal stability analysis of the governing Rayleigh equation, and typically for small to moderate radial wave numbers, the range of azimuthal wave numbers β, over which the flow is unstable increases for both a stretched and a shrinking disk, compared to the unstretched case. The inviscid absolute instability properties of the resulting base flows are also examined using spatiotemporal stability analysis. For suitably large stretching rates, the flow is absolutely unstable in only a small range of positive β. For small stretching rates there exists a second region of absolute instability for a range of negative β values. In this region the "effective" two-dimensional base flow, comprised of a linear combination of the radial and azimuthal velocity profiles that enter the Rayleigh equation calculation, has a critical point (unlike for $\beta > 0$) that can dominate the absolute instability growth rate contribution compared to the shear layer component. A similar behavior is found to occur for a radially shrinking disk, except these profiles have a strong shear layer structure and hence are more unstable than the stretching disk profiles. We thus find for a suitably large shrinking rate the absolute instability contribution from the critical point becomes subdominant to the shear layer contribution.

DOI: 10.1103/PhysRevFluids.2.073904

I. INTRODUCTION

There have been many theoretical, numerical, and experimental studies that have examined the flow of a rotating fluid above an infinite disk. The first theoretical investigation of this flow setup was due to Bödewadt [1]. Bödewadt calculated the steady boundary layer flow over an infinite stationary disk in the form of a similarity solution such that the flow is an exact solution of the Navier-Stokes equations. The steady flow itself is characterized by a radial pressure gradient that balances the centrifugal forces. This leads to a flow where fluid is pulled radially inward from infinity at the surface of the disk and ejected upward as it travels toward the center of the disk. This type of flow exemplifies a crossflow instability in a canonical example. This flow is relevant to industrial devices such as rotor-stator systems [2] and cavity elements of turbine engines [3]. The Bödewadt flow is not the only exact solution to the Navier-Stokes equations for rotating fluid flows that has received much attention. von Kármán [4] examined the steady flow produced by a rotating disk of infinite extent below a stationary fluid, while Ekman [5] examined a related flow where the disk and the outer flow are both rotating with almost equal angular velocities.

The content of this paper focuses on the Bödewadt flow, except with the added feature that the infinite disk is able to stretch, and we examine how the stability of the boundary layer is modified by stretching the disk beneath the rigidly rotating flow. We document the steady base flow shear stresses and velocity profiles as a function of the stretching (or shrinking) rate and investigate the convective instability (CI) and absolute instability (AI) properties of the resulting flows in the limit of large Reynolds number, where the Reynolds number is defined using the angular velocity of the

rotating flow. Hence we investigate how disk stretching or shrinking can control instability growth in the boundary layer and thus control the transition to turbulence.

Savaş [6,7] examined the stability of Bödewadt flow by conducting experiments on the spin-down flow of a cylindrical cavity. Savaş suggests that until secondary instabilities start to grow, this experimental setup is a suitable means to study the stability of Bödewadt flow. It was found that both stationary spiral modes (often referred to as type I instability) and unsteady circular instability modes appear. The circular modes propagate towards the center of the disk before dying out. Lopez and Weidman [8] confirmed the experimental results of Savaş [6,7] via direct axisymmetric numerical simulations and further experiments. By artificially allowing the sidewall of the cylinder to continue rotating even after the end walls stopped in their simulations, Lopez and Weidman found that the presence of the inwardly propagating circular modes could persist for longer times compared to when the sidewalls were stopped with the end walls. From this they concluded that the circular instability mode generation could persist indefinitely in the Bödewadt problem. The experimental results have also been confirmed via theoretical studies [9,10]. The inwardly propagating circular waves observed in the above experiments are of particular interest because, for the von Kármán boundary layer, Lingwood [11] discovered an AI consisting of a coalescence of an inviscidly unstable spiral mode and an inwardly propagating spatially decaying mode, similar to the circular modes described above. Based on this finding, Lingwood [12] conducted a linear stability analysis of the Bödewadt, Ekman, and von Kármán boundary layer flows, investigating the AI properties of each flow. A flow is absolutely unstable if when impulsively forced the response to the transient disturbance grows in time at the location where the forcing is applied. If the disturbance grows in time along a characteristic with nonzero speed but decays at the point at which it was forced, then the flow is convectively unstable [13]. Following the work of Briggs [14], the AI characteristics of a flow can be determined via a spatiotemporal stability analysis in which both the wave number and frequency of the flow are allowed to become complex. This is in contrast with a temporal or spatial analysis where only the frequency or wave number, respectively, is allowed to become complex [15]. The AI growth rate is calculated by searching for special saddle points in the complex wave-number plane, through which the inverse Fourier transform contour can pass. For each of the three above cited flows, Lingwood [12] calculated neutral stability contours, at finite Reynolds numbers, for the AI of the flows by transforming the governing linear partial differential equations into six first-order ordinary differential equations. Using a parallel flow assumption Lingwood also conducted inviscid AI calculations and found that the Bödewadt flow in particular was absolutely unstable for a range of both positive and negative azimuthal wave numbers of the instantaneous forcing.

In the present study we reexamine the inviscid CI and AI properties of the Bödewadt flow as well as for the new flows that incorporate a stretching or shrinking disk. In particular for the Bödewadt flow problem, we consider the AI of perturbations with azimuthal wave numbers $\beta < -0.3$ that are not present in [12]. Here we find that the growth rate of the AI reduces from its $\beta > 0$ maximum value, but for $\beta \lesssim -0.3$ the growth rate becomes dominated by an additional saddle point that produces a secondary maximum in the growth rate curve. It is shown that this additional saddle point has an "effective" two-dimensional velocity profile containing a critical point away from the surface of the disk. At this azimuthal wave number, the contribution to the AI from this critical point is larger than that of the shear layer interaction with the disk surface and hence its growth rate is larger. The same significant contribution from critical points on flow stability was shown for the von Kármán flow by Healey [16] in the long-wave-number limit. In the current work it is also shown that stretching the disk beneath the rotating flow tends to reduce the effect (both maximum growth rate and existence range of azimuthal wave numbers) of the AI, while shrinking the disk enhances the AI.

The present paper is laid out as follows. In Sec. II we derive the steady base flow equations as well as the governing ordinary differential equations for the inviscid linear stability analysis in the parallel flow limit. In Sec. III we present numerical solutions to the base flow equations and examine the asymptotic behavior in a region far from the surface of the disk. Convective and absolute instability results for the base flow profiles are given in Sec. IV with a discussion and concluding remarks given in Sec. V.

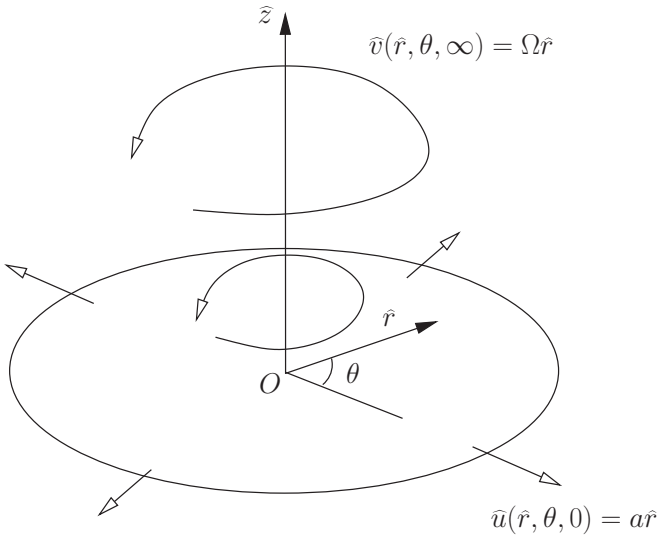

FIG. 1. Schematic diagram of the radially stretching disk below a rotating fluid.

II. FORMULATION

The problem we consider is a disk radially stretching at constant strain rate a in the dimensional $(\hat{x},\hat{y})$ plane, below a rigidly rotating fluid, which in the large-$\hat{z}$ far field is rotating steadily with constant angular velocity Ω. A schematic diagram of the physical setup is given in Fig. 1. The flow is governed in the inertial nonrotating reference frame by the incompressible Navier-Stokes equations

$$\frac{\partial\hat{\mathbf{u}}}{\partial\hat{t}}+\hat{\mathbf{u}}\cdot\boldsymbol{\nabla}\hat{\mathbf{u}}=-\frac{1}{\rho}\boldsymbol{\nabla}\hat{p}+\nu\nabla^2\hat{\mathbf{u}},\quad \boldsymbol{\nabla}\cdot\hat{\mathbf{u}}=0,$$

where $\hat{\mathbf{u}}$ is the dimensional fluid velocity, ρ is the fluid density, and ν is the kinematic viscosity. We use cylindrical polar coordinates $(\hat{r},\theta,\hat{z})$ to formulate the problem with corresponding velocity components $\hat{\mathbf{u}}=(\hat{u},\hat{v},\hat{w})$. The boundary condition on the surface of the disk located at $z=0$, oriented in the (x,y) plane, is $\hat{\mathbf{u}}=(a\hat{r},0,0)$ and in the far field $\hat{z}\to\infty$, $\hat{\mathbf{u}}\to(0,\Omega\hat{r},\hat{w}_\infty)$, where $\hat{w}_\infty$ is not prescribed but is found as part of the solution. The form of this boundary condition suggests seeking a solution for the base flow that is axisymmetric.

We nondimensionalize the problem by introducing the common scales $\sqrt{\nu/\Omega}$ for lengths, $\sqrt{\nu\Omega}$ for velocities, $1/\Omega$ for time, and $\rho\nu\Omega$ for pressure. Thus the dimensionless incompressible Navier-Stokes equations in the inertial reference frame are

$$u_t+uu_r+\frac{vu_\theta}{r}+wu_z-\frac{v^2}{r}=-p_r+u_{rr}+\frac{u_r}{r}+\frac{u_{\theta\theta}}{r^2}+u_{zz}-\frac{u}{r^2}-\frac{2v_\theta}{r^2},\tag{2.1a}$$

$$v_t+uv_r+\frac{vv_\theta}{r}+wv_z+\frac{uv}{r}=-\frac{p_\theta}{r}+v_{rr}+\frac{v_r}{r}+\frac{v_{\theta\theta}}{r^2}+v_{zz}-\frac{v}{r^2}+\frac{2u_\theta}{r^2},\tag{2.1b}$$

$$w_t+uw_r+\frac{vw_\theta}{r}+ww_z=-p_z+w_{rr}+\frac{w_r}{r}+\frac{w_{\theta\theta}}{r^2}+w_{zz},\tag{2.1c}$$

$$u_r+\frac{u}{r}+\frac{v_\theta}{r}+w_z=0,\tag{2.1d}$$

where (u,v,w) are the dimensionless velocity components, p is the dimensionless pressure, and (r,θ,z) are the dimensionless cylindrical polar coordinates. The subscripts in (2.1) denote partial

derivatives. In these nondimensional variables the disk boundary conditions are

$$u(r,\theta,0) = \sigma r, \quad v(r,\theta,0) = 0, \quad w(r,\theta,0) = 0 \tag{2.2a}$$

and the far-field conditions are

$$u(r,\theta,\infty) = 0, \quad v(r,\theta,\infty) = r, \quad w(r,\theta,\infty) = w_\infty, \tag{2.2b}$$

where w_∞ is to be determined. The parameter $\sigma = a/\Omega$ defines a one-parameter family of possible solutions.

A. Base flow

The flow can be separated into an axisymmetric steady base flow and a more general unsteady part whose amplitude is characterized by a small parameter $\delta \ll 1$. Thus inserting

$$u = rf'(z) + \delta\bar{u}(r,\theta,z,t), \tag{2.3a}$$

$$v = rg(z) + \delta\bar{v}(r,\theta,z,t), \tag{2.3b}$$

$$w = -2f(z) + \delta\bar{w}(r,\theta,z,t), \tag{2.3c}$$

$$p = P(r,z) + \delta\bar{p}(r,\theta,z,t) \tag{2.3d}$$

into (2.1) and (2.2) and equating terms at $O(1)$ leads to the coupled pair of nonlinear ordinary differential equations

$$f''' + 2ff'' - f'^2 + g^2 - 1 = 0, \tag{2.4a}$$

$$g'' + 2(fg' - f'g) = 0 \tag{2.4b}$$

to be solved together with the boundary conditions

$$f(0) = 0, \quad f'(0) = \sigma, \quad f'(\infty) = 0, \tag{2.5a}$$

$$g(0) = 0, \quad g(\infty) = 1. \tag{2.5b}$$

In (2.3c) the form of the base flow $-2f(z)$, is found by the need to satisfy (2.1d) and the primes in (2.4) denote ordinary derivatives with respect to z. In deriving the above system of ordinary differential equations it is also possible to compute the base pressure field

$$p(r,z) = p_0 + 2\sigma^2 + \tfrac{1}{2}r^2 - 2(f' + f^2), \tag{2.6}$$

where p_0 is the constant pressure at $(r,z) = (0,0)$. The governing ordinary differential equations (2.4) and the pressure field (2.6) can be shown to agree with (3.11)–(3.16) of [12] when the Rossby number $\mathrm{Ro} \equiv 1$. Note from (2.3c) that $w_\infty = -2f(\infty)$.

The radial and azimuthal dimensional shear stresses on the disk surface are given by

$$\tau_r = \rho\nu\Omega r f''(0), \quad \tau_\theta = \rho\nu\Omega r g'(0).$$

Numerical results for the base flow equations are investigated in Sec. III.

B. Linearized disturbance equations

Substituting (2.3) into (2.1) and equating terms of $O(\delta)$ furnishes the linearized disturbance equations

$$D\bar{u} + rf''\bar{w} + f'\bar{u} - 2g\bar{v} = -\bar{p}_r + L\bar{u} - \frac{\bar{u}}{r^2} - \frac{2\bar{v}_\theta}{r^2}, \tag{2.7a}$$

$$D\bar{v} + rg'\bar{w} + f'\bar{v} + 2g\bar{u} = -\frac{\bar{p}_\theta}{r} + L\bar{v} - \frac{\bar{v}}{r^2} + \frac{2\bar{u}_\theta}{r^2}, \tag{2.7b}$$

$$D\bar{w} - 2f'\bar{w} = -\bar{p}_z + L\bar{w}, \tag{2.7c}$$

$$\bar{u}_r + \frac{\bar{u}}{r} + \frac{\bar{v}_\theta}{r} + \bar{w}_z = 0, \tag{2.7d}$$

where

$$D \equiv \frac{\partial}{\partial t} - rf''\frac{\partial}{\partial r} + g\frac{\partial}{\partial \theta} - 2f\frac{\partial}{\partial z}, \quad L \equiv \frac{1}{r}\frac{\partial}{\partial r}\left(r\frac{\partial}{\partial r}\right) + \frac{1}{r^2}\frac{\partial^2}{\partial \theta^2} + \frac{\partial^2}{\partial z^2}.$$

These linear partial differential equations have coefficients that depend upon r and z but not on θ or t and therefore we can take Fourier and Laplace transforms respectively. However, since the resulting disturbance equations remain as partial differential equations in r and z, they can only be reduced to ordinary differential equations at leading order by considering a point on the disk far from the flow axis of rotation where the boundary layer profile is assumed to be approximately parallel. For the stability analysis presented in this paper we will work in this limiting regime.

If we let $\hat{R}$ be the dimensional radial position at which we perform a stability analysis of the flow on the disk, then we can introduce the Reynolds number Re such that

$$\mathrm{Re} = \hat{R}\sqrt{\frac{\Omega}{\nu}}.$$

We next introduce a new scaled radial coordinate $\tilde{r}$ given by

$$r = \tilde{r}\,\mathrm{Re},$$

where we assume $\mathrm{Re} \gg 1$, to be far from the flow axis of rotation, and $\tilde{r} = O(1)$ in this region. In this region we neglect the weak nonparallel effects of the boundary layer on the disk and hypothesize that the disturbance quantities assume the waveform given by

$$\bar{u}(\tilde{r},\theta,z,t) = u(z)\exp[i\,\mathrm{Re}(\alpha\tilde{r} + \bar{\beta}\theta - \omega t)], \tag{2.8a}$$

$$\bar{v}(\tilde{r},\theta,z,t) = v(z)\exp[i\,\mathrm{Re}(\alpha\tilde{r} + \bar{\beta}\theta - \omega t)], \tag{2.8b}$$

$$\bar{w}(\tilde{r},\theta,z,t) = w(z)\exp[i\,\mathrm{Re}(\alpha\tilde{r} + \bar{\beta}\theta - \omega t)], \tag{2.8c}$$

$$\bar{p}(\tilde{r},\theta,z,t) = \mathrm{Re}\,p(z)\exp[i\,\mathrm{Re}(\alpha\tilde{r} + \bar{\beta}\theta - \omega t)]. \tag{2.8d}$$

Here α and $\bar{\beta}$ are $O(1)$ scaled radial and azimuthal wave numbers, respectively, ω is the scaled angular frequency, and we have recycled the notation (u,v,w,p) with the understanding that henceforth these refer only to the perturbation quantities. The presence of the Reynolds number in the exponential terms indicates that the resulting waves are short compared to the distance to the axis of rotation for the flow field. Thus this is the basis for the WKB approximation in (2.8).

Substituting (2.8) into the linearized disturbance equations (2.7) and taking the limit as $\mathrm{Re} \to \infty$ leads to four ordinary differential equations for (u,v,w,p), which, on eliminating (u,v,p), reduce to the Rayleigh equation

$$(Q - \omega)(w'' - \gamma^2 w) - Q''w = 0, \tag{2.9a}$$

where

$$Q(z) = \alpha f'(z) + \beta g(z), \quad \gamma^2 = \alpha^2 + \beta^2, \tag{2.9b}$$

$\beta = \bar{\beta}/\tilde{r}$, and the primes denote derivatives with respect to z. Note that $\mathrm{Re}\bar{\beta}$ is an integer, but as we are working in the large-Re limit we can consider β to be a real variable. While the disturbance equation does not depend explicitly on r through the Reynolds number, there is still a radial dependence on the solutions through the quantity β. The wave number α and/or the frequency ω are allowed to become complex in order to satisfy the homogeneous boundary conditions

$$w(0) = 0, \quad w(\infty) = 0. \tag{2.10}$$

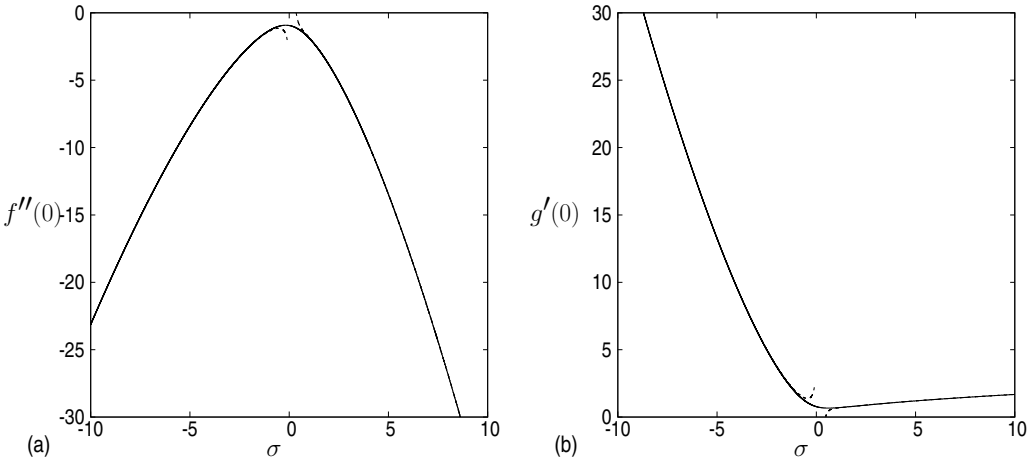

FIG. 2. Plot of the numerical shear stresses (a) $f''(0)$ and (b) $g'(0)$ as a function of σ given by the solid lines and the three-term asymptotic expansions (3.1) and (3.2) given by the dashed lines.

Hence we perform both a temporal and spatiotemporal stability analysis of (2.9) in Sec. IV, calculating α and ω such that (2.10) is satisfied.

III. NUMERICAL SOLUTIONS FOR THE BASE FLOW

In this section we present numerical results for the solution to the one-parameter system given by (2.4) and (2.5). The system is solved using a fourth-order Runge-Kutta shooting method with Newton iterations at $z = z_{\max}$ to update the values of $f''(0)$ and $g'(0)$ such that the far-field boundary conditions are satisfied (see [17]). The integration domain $z \in [0, z_{\max}]$ and the integration step size are varied to ensure that the results presented here are independent of these parameters. We find that $z_{\max} = 20$ is large enough to correctly capture the far-field boundary conditions. The resulting values of $f''(0)$ and $g'(0)$ as a function of σ are shown in Fig. 2. The radial shear stress $f''(0)$ is always negative, while the azimuthal shear stress $g'(0)$ is always positive for both stretching ($\sigma > 0$) and shrinking ($\sigma < 0$) disks. However, both shear stresses exhibit extrema at $\sigma \approx 0$, which corresponds to the Bödewadt problem. The $|\sigma| \gg 1$ asymptotic forms of the shear stresses are given by

$$f''(0) = \sigma^{3/2}[F_{0Z}(0) + \sigma^{-2}F_{2ZZ}(0) + \sigma^{-4}F_{4ZZ}(0)] + O(\sigma^{-9/2}), \tag{3.1a}$$

$$g'(0) = \sigma^{1/2}[G_{0Z}(0) + \sigma^{-2}G_{2Z}(0) + \sigma^{-4}G_{4Z}(0)] + O(\sigma^{-11/2}) \tag{3.1b}$$

for $\sigma > 0$ and

$$f''(0) = |\sigma|^{3/2}[\tilde{F}_{0ZZ}(0) + |\sigma|^{-1}\tilde{F}_{2ZZ}(0) + |\sigma|^{-2}\tilde{F}_{4ZZ}(0)] + O(|\sigma|^{-3/2}), \tag{3.2a}$$

$$g'(0) = |\sigma|^{3/2}[\tilde{G}_{0Z}(0) + |\sigma|^{-1}\tilde{G}_{2Z}(0) + |\sigma|^{-2}\tilde{G}_{4Z}(0)] + O(|\sigma|^{-3/2}) \tag{3.2b}$$

for $\sigma < 0$ and are plotted as the dashed lines in Fig. 2. The values of the coefficients are given along with the asymptotic analysis in Appendix A.

The corresponding radial and azimuthal velocity profiles $f'(z)$ and $g(z)$ are plotted in Fig. 3 for integer values of σ between -4 and 4. For $\sigma > 0$, $g(z)$ has a simple boundary layer structure, increasing from zero at the disk to its far-field value $g = 1$. There are in fact small oscillations about $g = 1$ as $z \to \infty$, but these are not visible in the figure (see Sec. III). The radial velocity $f'(z)$ behaves similarly, decreasing in magnitude from its value at the disk, σ, to $f' = 0$ as $z \to \infty$. These

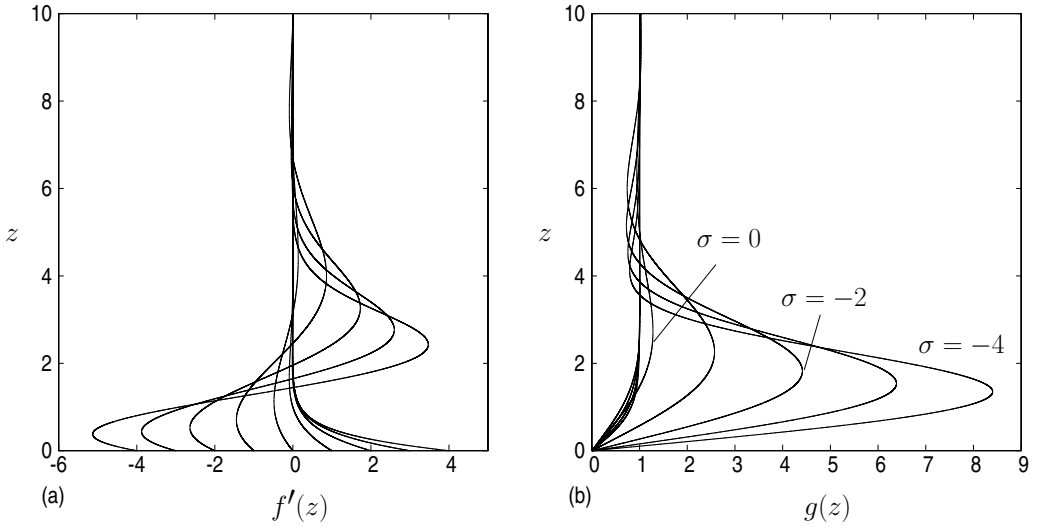

FIG. 3. Plot of the velocity profiles (a) $f'(z)$ and (b) $g(z)$ for integer values of σ between -4 and 4.

profiles are similar to those presented in [18], which studied the Bödewadt problem with an imposed Navier slip condition at the wall, where the velocity at the wall is given as a multiple of the shear value at the wall and thus is found as part of the solution procedure.

For $\sigma \leqslant 0$, on the other hand, $g(z)$ exhibits a strong wall jet structure in the boundary layer, the magnitude of which increases as σ decreases, while $f'(z)$ now includes a region of reverse flow at the disk. In both cases the oscillations as $z \to \infty$ are now obvious. In order to accurately capture these oscillations at infinity, it is necessary to compute results to a high degree of precision. For $-5 \lesssim \sigma \lesssim 1$ we find that quadruple precision is required to accurately integrate out to $z = 20$. Outside this region double precision is sufficient to produce the required accuracy. Due to the reverse flow at the surface of the disk, we expect the results for $\sigma \leqslant 0$ to be more unstable (both convectively and absolutely) than those for $\sigma > 0$. However, the actual stability properties depend on the form of the effective two-dimensional profile $Q(z)$ in (2.9b), thus determining the stability properties is difficult without first knowing the form of $Q(z)$. Before performing the stability analysis, we first highlight the large-z behavior of the base flow, which highlights the difficulty in solving the base flow, but also allows for an alternative means for calculating the base flow, integrating from $z = \infty$ to the disk.

Oscillatory behavior at large z

It is possible to determine the asymptotic behavior of the velocity profile at large z by writing

$$g(z) = 1 + \delta\tilde{g}(z), \quad f(z) = f_\infty + \delta\tilde{f}(z), \tag{3.3}$$

where δ is a small parameter and $f_\infty = f(\infty)$. Substituting these expressions into (2.4) and retaining only terms at $O(\delta)$ leads to the pair of equations

$$\tilde{f}''' + 2f_\infty\tilde{f}'' + 2\tilde{g} = 0, \tag{3.4a}$$

$$\tilde{g}'' + 2f_\infty\tilde{g}' - 2\tilde{f}' = 0. \tag{3.4b}$$

Substituting (3.4b) into (3.4a) and simplifying leads to the fourth-order ordinary differential equation for $\tilde{g}(z)$,

$$\tilde{g}^{(iv)} + 4f_\infty\tilde{g}''' + 4f_\infty^2\tilde{g}'' + 4\tilde{g} = 0. \tag{3.5}$$

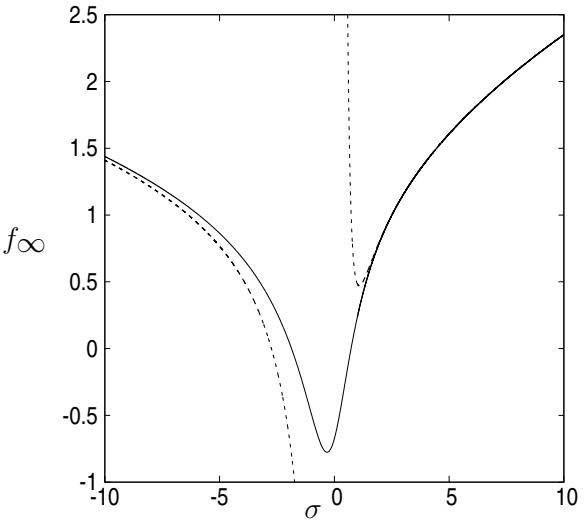

FIG. 4. Plot of the constant $f_\infty = f(\infty)$ from the numerical solution as a function of σ. The dashed lines represent the large $|\sigma|$ asymptotic results from Appendix A.

Solving this equation and retaining only those terms that tend to zero as $z \to \infty$ gives

$$\tilde{g}(z) = e^{\lambda_r z}(A \cos \lambda_i z + B \sin \lambda_i z), \tag{3.6a}$$

where A and B are constants that are in principle determined by the boundary conditions at the disk and

$$\lambda_r = -f_\infty - \frac{1}{2}\sqrt{2f_\infty^2 + 2\sqrt{f_\infty^4 + 4}}, \quad \lambda_i = \frac{2}{\sqrt{2f_\infty^2 + 2\sqrt{f_\infty^4 + 4}}}. \tag{3.6b}$$

It is clear from the form of $\lambda_r < 0$ and $\lambda_i > 0$ that the constant f_∞ is important in determining the large-z behavior and is plotted in Fig. 4.

The exponential form of the solution in (3.6a) and the quadratic nonlinearities that appear in (2.4) suggest that the large-z form can be approximated by expanding in powers of $\exp(\lambda_r z)$, essentially $\delta = 1$ in (3.3), and $\exp(\lambda_r z)$ becomes the small component of the expansion. The first few terms in the expansion for $g(z)$ are

$$g(z) \sim 1 + e^{\lambda_r z}(A \cos \lambda_i z + B \sin \lambda_i z) + e^{2\lambda_r z}(\alpha + \beta \cos \lambda_i z + \gamma \sin \lambda_i z), \tag{3.7}$$

where the forms of α, β, and γ are given in Appendix B. The corresponding form of $f(z)$ can be found using (3.4b), but as it is not required for the subsequent analysis, we do not express its full form here.

The undetermined constants A and B in (3.7) are found from the numerical solution by matching the position of the stationary points, z_m of $\tilde{g}$, and the value of the function $\tilde{g}_m = \tilde{g}(z_m)$ at these points. This furnishes a pair of equations at each stationary point that can be solved to give

$$A = \frac{\tilde{g}_m e^{-\lambda_r z_m}}{\lambda_i}(\lambda_i \cos \lambda_i z_m + \lambda_r \sin \lambda_i z_m), \quad B = \frac{\tilde{g}_m e^{-\lambda_r z_m}}{\lambda_i}(\lambda_i \sin \lambda_i z_m - \lambda_r \cos \lambda_i z_m). \tag{3.8}$$

Performing this calculation at each stationary point, we find that the values of A and B converge as the value of z_m increases, at least to four or five significant figures, which we find to be sufficient for graphical accuracy. The large-z form of $g(z)$ (3.7) is plotted together with the numerical solution for $\sigma = \{5, 0, -5\}$ in Fig. 5. The values of A and B for these results are given in Table I. We have found

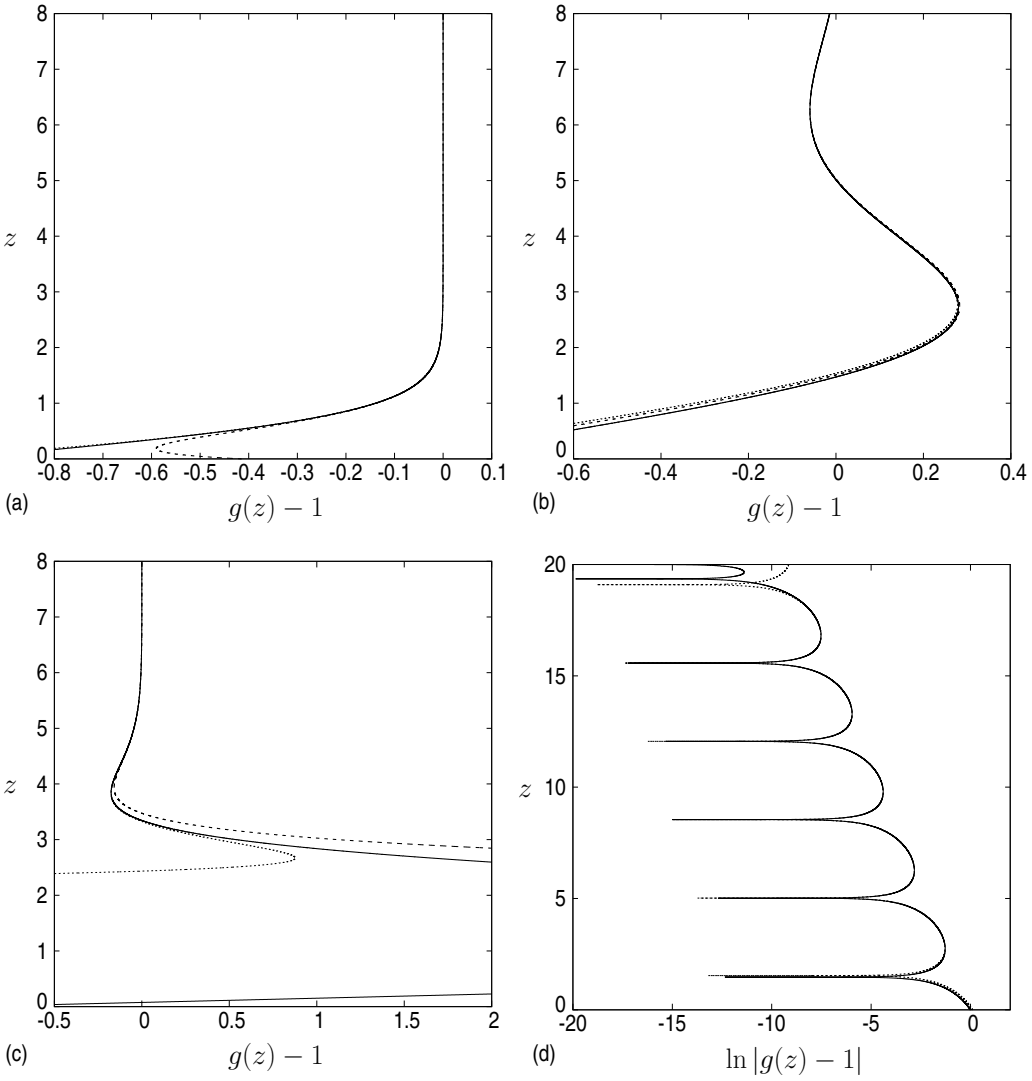

FIG. 5. Plot of the azimuthal velocity $g(z) - 1$ for (a) $\sigma = 5$, (b) $\sigma = 0$, and (c) $\sigma = -5$. In each panel the numerical solution is given by the solid line and the two-term and three-term asymptotic results from (3.7), which are given by the dashed line and dotted line, respectively. (d) Plot of $\ln|g(z) - 1|$ to better show the agreement between the numeric and asymptotic solution for $\sigma = 0$. Here only the three-term asymptotic result is plotted.

TABLE I. Table of values of A and B from (3.6) used in Fig. 5.

σ	A	B
–5	346.0600	1377.75896
0	−1.04752	0.23777
5	−0.41458	−6.28651

in our study that correctly determining these far-field oscillations is important when undertaking the stability analysis, in the subsequent section.

IV. STABILITY PROPERTIES OF BASE FLOW PROFILES

A. Convective instability

To investigate the effect of the stretching disk on the CI properties of the flow, we consider a temporal stability analysis of (2.9) for the real values of the radial wave number $\alpha = 0.2$, 0.4, and 0.8. The values of $\alpha = 0.2$ and 0.4 are in the parameter region where the Bödewadt flow is highly convectively unstable, while $\alpha = 0.8$ lies at the edge of the instability region. The stability properties are found by solving the dispersion relation $\Delta(\alpha,\omega;\beta,\sigma) = 0$, where $\Delta(\alpha,\omega;\beta,\sigma) = w(\infty;\alpha,\omega;\beta,\sigma)$ is found by solving (2.9) for a given base velocity profile $Q(z)$ ensuring the boundary condition (2.10) at $z = \infty$ is satisfied. This quantity equals zero when the correct value of ω is chosen for a given α. The dispersion relation is solved using the same shooting process as used for the base flow. In this section we investigate how the range of azimuthal wave numbers β over which the flow is unstable [$\mathrm{Im}(\omega) = \omega_i > 0$] varies with σ. In a CI analysis we are interested in the growth of individual waves, not their interaction with each other.

In Figs. 6(a) and 6(b) we plot the growth rate ω_i for the CI with $\alpha = 0.2$ for $\sigma \geqslant 0$ and $\sigma \leqslant 0$, respectively. The results show for this wave number that, as expected, due to the increased amount of reverse flow at the surface of the disk for $\sigma \leqslant 0$ (see Fig. 3), the growth rate is larger than the $\sigma = 0$ result. In fact, as Fig. 7(a) shows, for $\sigma \leqslant 0$ the amount of shear in the base flow $Q(z)$ [here we plot $Q(z)/\alpha = f'(z) + \frac{\beta}{\alpha} g(z)$] is greater than the Bödewadt flow for all values of β/α plotted, while the converse is true for the stretched disk $\sigma > 0$.

As for the range of β values exhibiting a CI, we first observe that the stability results consist of multiple unstable modes, two of which exchange their dominance in the flow at $\beta = 0.385$ for $\sigma = 0$, which is seen by the discontinuity in gradient of ω_i in Fig. 6(a). In Fig. 7(b) we plot $|w|$ for each of these modes at $\alpha = \beta = 0.2$ for $\sigma = 0$. Here the dominant mode has a mode shape with maximum value close to the disk at $z = 2.8835$. When we compare this with the solid line for the $\alpha/\beta = 1$ result in Fig. 7(a) we observe this maximum occurring at the edge of the lower shear layer in $Q(z)$. The subdominant mode in Fig. 7(b) has its maximum at $z = 6.3985$, which corresponds to the edge of the second shear layer of $Q(z)$. Therefore, we note that both shear layers are contributing to the stability of the flow, with the lower shear layer contribution dominating over the majority of the instability region and the upper shear layer dominating for larger β values.

So for $\sigma < 0$ the range of β values for the existence of the CI increases from the Bödewadt result, albeit after an initial decrease in size for $0 > \sigma \geqslant -0.5$, and the value of β at which the maximum growth rate occurs also decreases. For $\sigma > 0$ in Fig. 6(a) the maximum value of the growth rate moves to larger values of β but interestingly, the maximum value of ω_i decreases from $\sigma = 0$ to $\sigma = 1$ and then increases at $\sigma = 2$. The overall range of β values for which there is an instability increases as σ is increased, but note that ω_i for $\beta < 0$ reduces to small values by $\sigma = 2$; thus observing these modes at this parameter value in a set of spin-down experiments similar to those of Savaş [6,7] would be difficult.

For $\alpha = 0.5$ in Figs. 6(c) and 6(d) a similar behavior is observed as for the $\alpha = 0.2$ case. Here the range of β values over which an instability exists increases for both $\sigma > 0$ and $\sigma < 0$ compared to the Bödewadt result. The significant difference at this wave number is the rate at which the maximum value of ω_i increases for $\sigma < 0$ and decreases for $\sigma > 0$ is much larger than for $\alpha = 0.2$. Also note that here the maximum value of ω_i continues to decrease at $\sigma = 2$, unlike in the $\alpha = 0.2$ case, thus showing that the form of $Q(z)$ for $\sigma = 2$ is more unstable to long waves (small α) but more stable to shorter waves (larger α).

For $\alpha = 0.8$ in Fig. 6(e) it is a different story. Here the size of the azimuthal wave-number region is approximately constant for the different values of σ considered, but the position of the instability region varies. We note here that the corresponding results for $\sigma = 2$, -1, and -2 are stable.

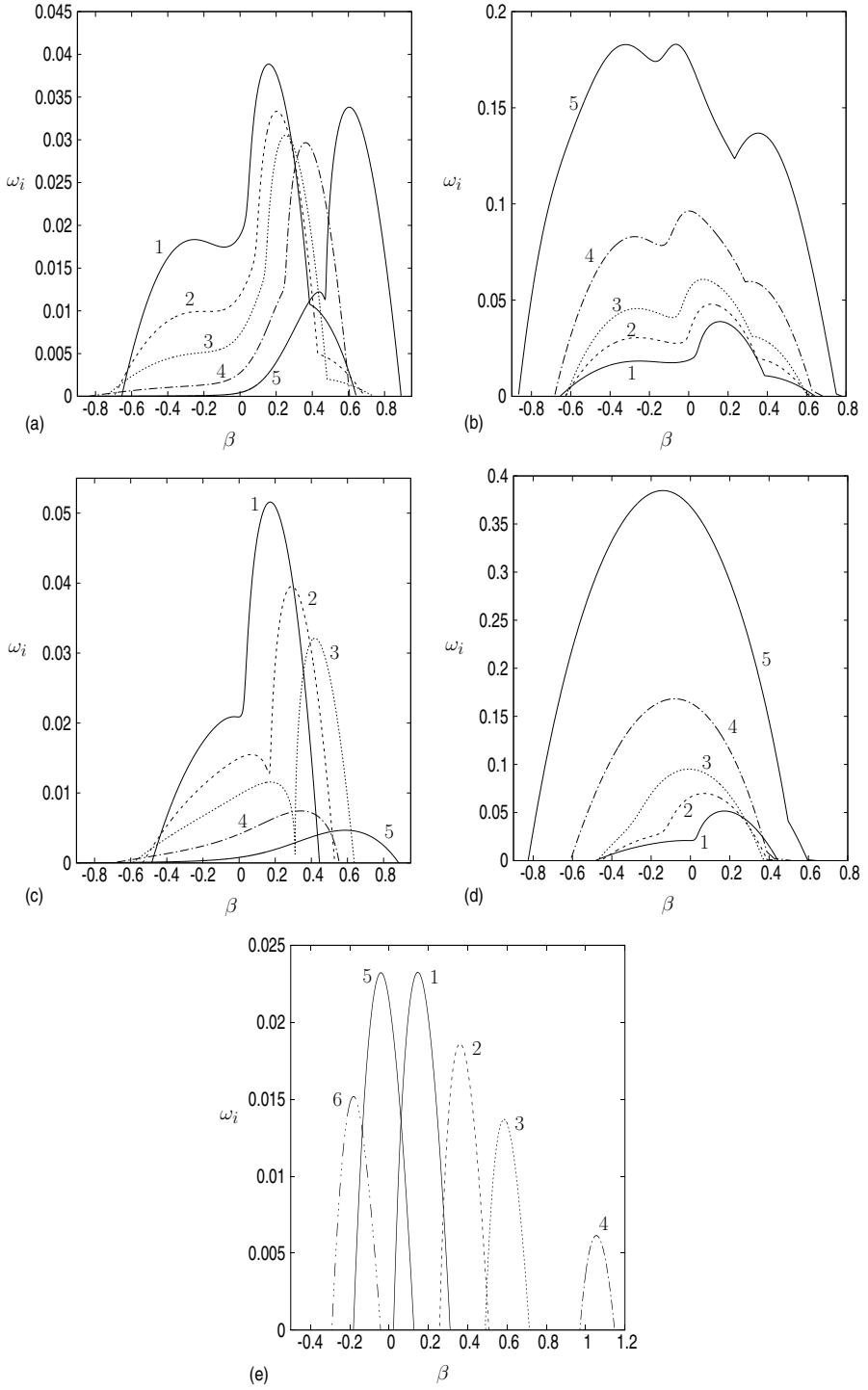

FIG. 6. Plots of the temporal stability growth rates $\omega_i(\beta)$ for (a) and (b) $\alpha = 0.2$, (c) and (d) $\alpha = 0.5$, and (e) $\alpha = 0.8$. In (a) and (c) the lines $\sigma = \{0, 0.25, 0.5, 1, 2\}$ are labeled 1–5 respectively, in (b) and (d) the lines $\sigma = \{0, -0.25, -0.5, -1, -2\}$ are labeled 1–5 respectively, and in (e) the lines $\sigma = \{0, 0.25, 0.5, 1, -0.25, -0.5\}$ are labeled 1–6, respectively.

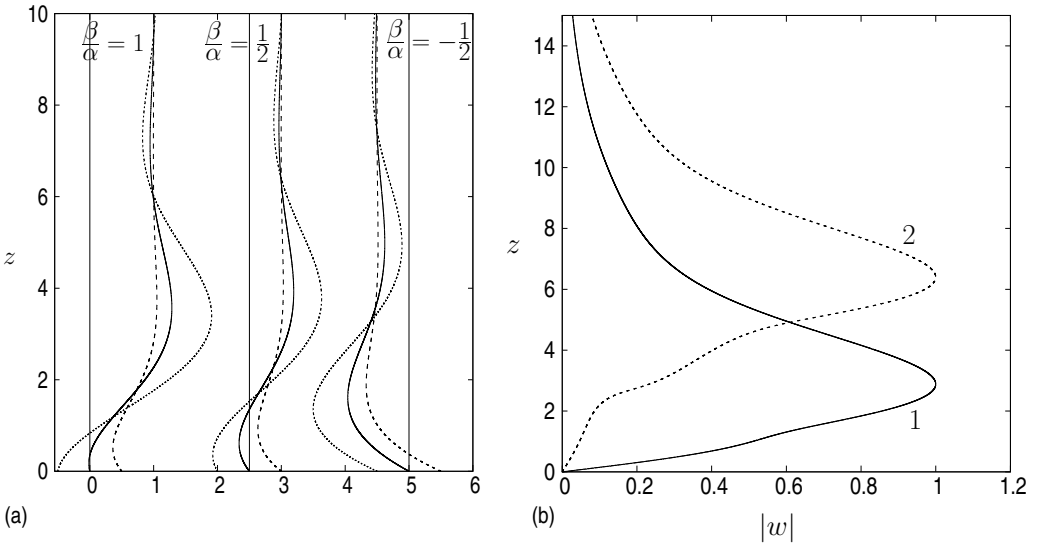

FIG. 7. (a) Plot of $f'(z) + \frac{\beta}{\alpha} g(z)$ for $\frac{\beta}{\alpha} = \{1, 1/2, -1/2\}$ The three cases are separated by a constant and in each case the solid line represents $\sigma = 0$, the dashed line represents $\sigma = 0.5$, and the dotted line represents $\sigma = -0.5$. (b) Plot of $|w|$ for $\alpha = \beta = 0.2$ and $\sigma = 0$. Result 1 represents the dominant eigenmode with $\omega = 0.0725 + 0.0278i$, while result 2 gives the subdominant eigenmode with $\omega = 0.2312 + 0.0094i$.

The results in this section indicate that the region of azimuthal wave numbers for CI typically increases for a small to moderate fixed value of α when the disk is both stretched ($\sigma > 0$) and shrunk ($\sigma < 0$). The corresponding behavior for AI is considered in Sec. IV B with particular interest in how individual modes interact with one another.

B. Absolute instability

While the CI of a flow depends on the stability of individual waves, its AI is a consequence of the interaction of these waves as they propagate as wave packets. The calculation of the response of the base flow to infinitesimal perturbations in a frame of reference fixed on the disturbance position for both the Bödewadt and Ekman layer flows can be found in [12] and for the von Kármán flow in [11]. We apply the same fundamental approach to the base flows in this paper.

Absolute instabilities of the flow correspond to *special* saddle points of the dispersion relation $\Delta(\alpha,\omega;\beta,\sigma) = 0$ that satisfy the Briggs criteria for AI [12,14,19–22] and the position of the saddle points are found by simultaneously solving $\Delta(\alpha,\omega;\beta,\sigma) = \Delta_\alpha(\alpha,\omega;\beta,\omega) = 0$. Note here that both α and ω are typically complex.

In Fig. 8 we plot (a) $\omega_r(\beta)$, (b) $\omega_i(\beta)$, (c) $\alpha_r(\beta)$, and (d) $\alpha_i(\beta)$ when $\sigma > 0$ for the dominant saddle point for values of β where the flow is absolutely unstable. Here the stretching parameter takes the values $\sigma = \{0, 0.25, 0.5, 1, 2\}$. The result for $\sigma = 0$ is the Bödewadt result presented in Figs. 9(b) and 9(d) of [12] (denoted by the Rossby number Ro = 1). We note that while our results are in good agreement with those of [12] for $\beta > 0$, we obtain subtly different results for $\beta < 0$. However, our results are qualitatively similar to those of [12] when the Rossby number therein is Ro = 0.9 and 0.8 in the range $-0.3 \leqslant \beta \leqslant 0$. We believe this discrepancy is due to the difficulty in accurately calculating the base flow for this value of σ, as described in Sec. III. The fact that our results demonstrate qualitative agreement in behavior with the Ro = 0.9 and 0.8 results of [12] gives us confidence in our numerical procedure.

The Bödewadt result has a maximum growth rate at $\beta = 0.1871$ and the AI extends over the range of azimuthal wave numbers $\beta \in [-0.6659, 0.4605]$. At $\beta = -0.4096$ there exists a second,

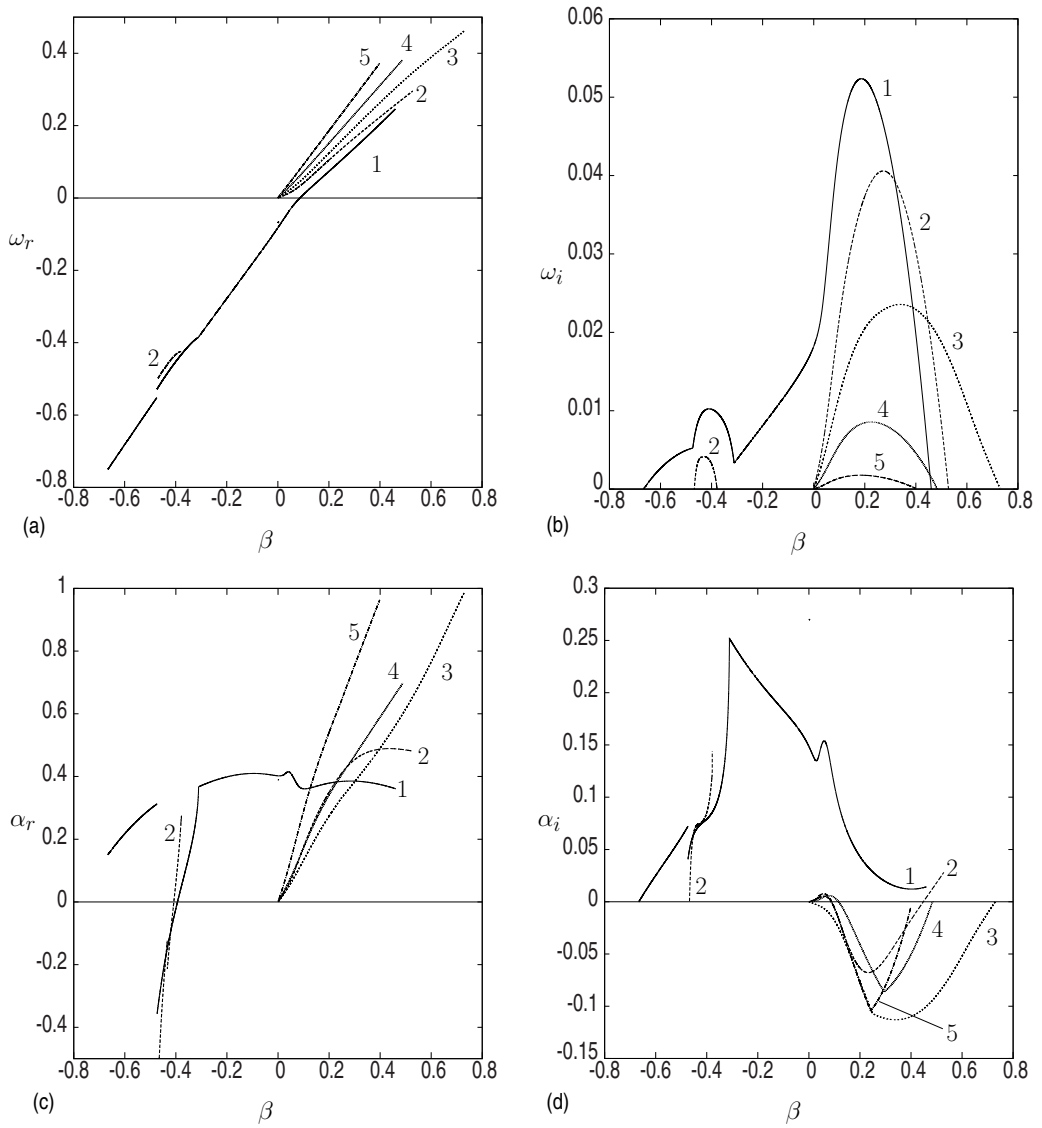

FIG. 8. Plots of (a) $\omega_r(\beta)$, (b) $\omega_i(\beta)$, (c) $\alpha_r(\beta)$, and (d) $\alpha_i(\beta)$ for $\sigma = \{0,0.25,0.5,1,2\}$ labeled 1–5, respectively.

smaller, maximum growth rate that is caused by a second saddle point on the inversion contour becoming the dominant saddle point. As the disk stretching rate is increased to $\sigma = 0.25$ the two maximum growth rate values decrease in magnitude and in fact the AI actually vanishes for a range of β values between these two maxima. The two maxima move to $\beta = 0.2725$ and $\beta = -0.4364$, respectively, and the flow is absolutely unstable for azimuthal wave numbers $\beta \in [-0.4673, -0.3785] \cup [0.0001,0.5280]$. As σ increases to 0.5, the flow is no longer absolutely unstable for $\beta < 0$, but the positive range of β for which an AI exists is larger still. Beyond this value, the range of β values for the AI decreases and for $\sigma = 2$ the flow is only absolutely unstable for $\beta \in [0,0.3991]$, but this instability is weak, with a maximum growth rate of $\omega_i = 1.773 \times 10^{-3}$. Note that this result is in contrast to the CI result in Fig. 6, which shows that the range of β values

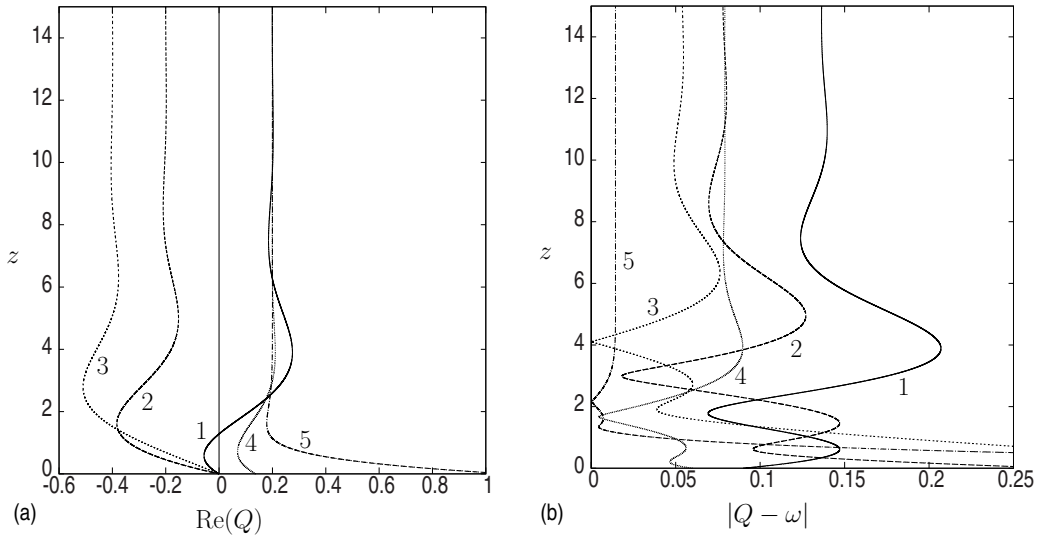

FIG. 9. Plot of (a) Re[$Q(z)$] and (b) $|Q(z)-\omega|$ labeled 1–5, respectively, for $(\sigma,\beta)=\{(0,0.2),(0,-0.2),(0,-0.4),(0.5,0.2),(2,0.2)\}$.

for CI increases as σ is increased from $\sigma=0$, and at $\sigma=2$, the magnitude of ω_i for the CI is much larger.

In Fig. 9(a) we plot $\mathrm{Re}(Q)=\alpha_r f'+\beta g$, which is the velocity profile that gives the AI, for $(\sigma,\beta)=\{(0,0.2),(0,-0.2),(0,-0.4),(0.5,0.2),(2,0.2)\}$. These profiles show a boundary layer shear flow structure for $\sigma=0$, with the maximum value of $\mathrm{Re}(Q)$ close to the surface of the disk increasing and moving upward as β is reduced. As σ is increased for fixed $\beta=0.2$ we observe that the shear layer structure of the base flow profile for an AI is reduced and this coincides with the flow becoming less absolutely unstable. If we examine $|Q-\omega|$ for the same profiles in Fig. 9(b), we now observe why for $(\sigma,\beta)=(0,-0.4)$ there is an increase in the growth rate ω_i as β is reduced for $\sigma=0$. This result [label 3 in Fig. 9(b)] has a critical point at $z_c=4.1026$ and this critical point makes an additional contribution to the AI of the flow [16]. Healey [16] demonstrates for the von Kármán rotating disk boundary layer, in the long-wave limit, that the contribution of a critical point (a second critical point in that case) dominates the AI properties for small β values. A similar phenomenon is occurring here, except it is the appearance of a critical point in $Q(z)$ as β is reduced, for $\sigma=0$, that is responsible for the additional increase in AI growth rate. When the critical point exists in $Q(z)$, it is likely that nonlinearity will first occur close to this critical point in the inviscid theory. The result plotted as label 5 in Fig. 9(b) also appears to exhibit a critical point at $z\approx 2$; however this is merely a point with a small value of $|Q-\omega|$ and not a critical point with $Q=\omega$. This is why the flow stability properties for these parameters are similar to those for other base flows with $\beta>0$. Note that, for profiles with a critical point, we modify our numerical scheme to integrate up to the critical layer and then jump to the other side without modifying w or dw/dz. We can do this because we consider the critical layer to be nonlinear and not viscous [23].

The growth rate curves in Fig. 10(b) demonstrate that as σ is decreased from zero the growth rate ω_i typically increases for all values of β, as was the case for the CI, except again at the edges of the stability domain, for $\sigma\in[-0.5,0]$. For $\sigma=-0.5$ this instability range is $\beta\in[-0.6219,0.4328]$. The maximum value of the growth rate increases as σ decreases and when $\sigma=-0.5$, $\omega_i=0.092\,38$, which is almost twice the maximum value when $\sigma=0$.

The base velocity profiles $\mathrm{Re}(Q)$ in Fig. 11(a) show that the AI in this parameter regime is dominated by the size of the shear layer within the boundary layer. For $(\sigma,\beta)=(-0.5,-0.4)$ (label 3) in Fig. 11(b) we again observe a critical point at $z_c=3.6078$ that dominates the AI properties of

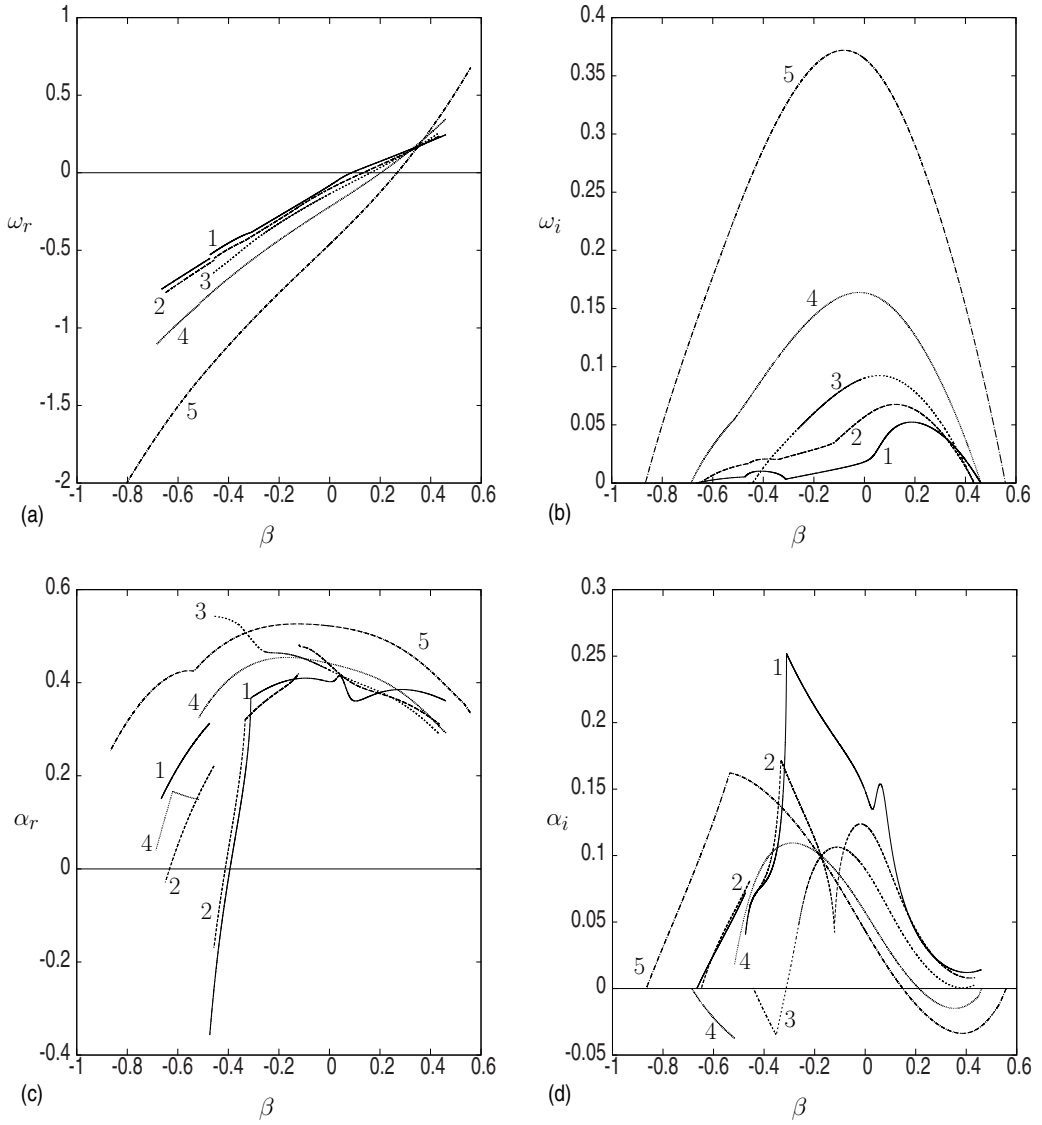

FIG. 10. Plots of (a) $\omega_r(\beta)$, (b) $\omega_i(\beta)$, (c) $\alpha_r(\beta)$, and (d) $\alpha_i(\beta)$ labeled 1–5, respectively, for $\sigma = \{0, -0.25, -0.5, -1, -2\}$.

the flow, over the shear layer magnitude. However, as σ is reduced further the critical point moves towards the disk until its contribution to the AI of the flow becomes subdominant to the contribution from the shear layer. This is seen to have occurred by $\sigma = -2$ in Fig. 11(b) for $\beta = -0.4$.

V. DISCUSSION AND CONCLUSIONS

In this paper we examined the flow generated by the linear radial stretching of a disk below a rotating fluid with constant angular velocity Ω and kinematic viscosity ν. We studied both the velocity profiles of the steady base flow and the inviscid CI and AI properties of this flow to infinitesimal perturbations via linear stability theory. The steady base flow was nondimensionalized and solely characterized by a single nondimensional parameter $\sigma = a/\Omega$, where a is the radial rate

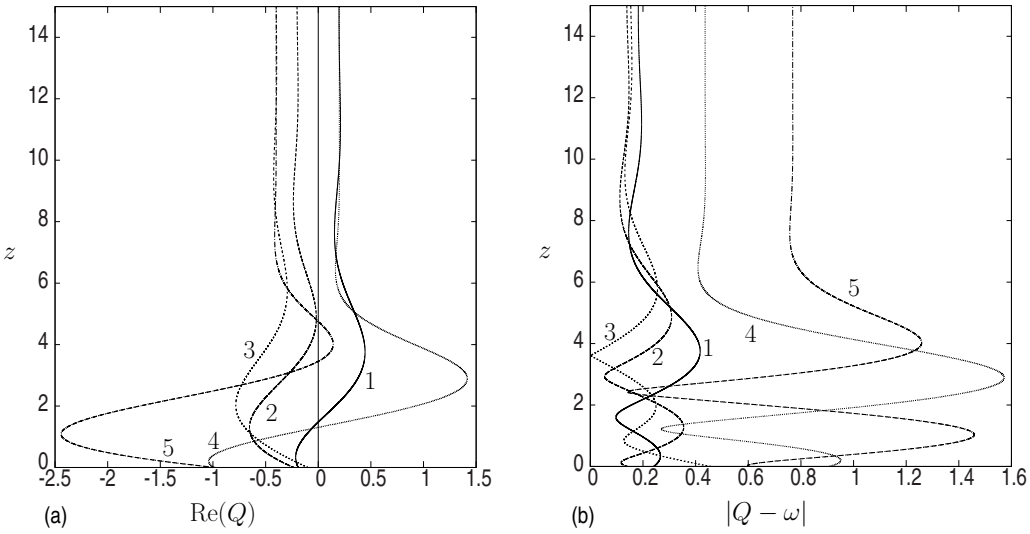

FIG. 11. Plots of (a) Re$[Q(z)]$ and (b) $|Q(z)-\omega|$ labeled 1–5, respectively, for $(\sigma,\beta)=\{(-0.5,0.2),(-0.5,-0.2),(-0.5,-0.4),(-2,0.2),(-2,-0.4)\}$.

of strain of the disk. Numerical results of the base flow equations showed that the radial component of the shear stress on the disk is always directed towards the origin, while the azimuthal component of the disk shear stress is directed in the positive θ direction.

For $\sigma \gtrsim 1$ the radial velocity component consisted of a velocity profile that obtained its maximum value at the surface of the disk and decreased to zero outside the boundary layer, while the azimuthal component was zero at the disk and increased to a unit value outside the boundary layer. For $\sigma \lesssim -1$, on the other hand, the radial velocity profile consisted of a shear layer profile with a region of reverse flow at the disk, while the azimuthal component had a wall jet structure with its maximum velocity confined to the boundary layer. For $-1 \lesssim \sigma \lesssim 1$ the flow transitioned between these two states. In particular, the case $\sigma = 0$ is the problem studied by Bödewadt [1]. For all values of σ the flow was shown to have oscillations outside the boundary layer that decay as $z \to \infty$. These oscillations are small for $\sigma > 0$ and more visible for $\sigma \leqslant 0$ and it was found that accurately calculating these oscillations was important in the subsequent stability analysis.

By considering infinitesimal perturbations of the base flows we examined the inviscid stability properties of the flow, in particular AI properties, to investigate the potential of the stretching disk to enhance or inhibit transition. We considered the stability of the flow at large radii, such that the flow is assumed to act parallel to the disk, so that nonparallel contributions to the stability calculation are neglected. For $\sigma = 2$ the flow was found to be absolutely stable except for a small region of azimuthal wave numbers $\beta \in [0,0.3991]$, where the magnitude of the AI growth rate was determined by the magnitude of the shear layer in the effective two-dimensional velocity profile $Q(z) = \alpha f'(z) + \beta g(z)$. As σ was reduced the growth rate increased and eventually a second instability region was found to exist for $\beta < 0$ [see Fig. 8(b)] where the magnitude of the growth rate was determined by the contribution of a critical point that occurs in $Q(z)$. Note that a critical point does not occur for $\beta > 0$. As σ is decreased further the AI due to the shear layer grows in both magnitude and the range of β values for which it exists and ultimately dominates the whole instability range when $\sigma = -2$. For this value of σ the AI velocity profiles with a critical point still exist and produce an AI, but they are subdominant to the shear layer contribution. The CI results are in accord with the AI results for $\sigma \leqslant 0$, but for $\sigma \geqslant 0$ the existence region for the CI increases with increasing σ, at least up to $\sigma = 2$, considered here.

ACKNOWLEDGMENTS

The authors would like to thank the anonymous referees, whose comments have led to an improved version of this paper.

APPENDIX A: ASYMPTOTIC ANALYSIS FOR $|\sigma| \gg 1$

In this appendix we consider the asymptotic form of the base flow for large disk stretching and shrinking rates $|\sigma|$. We consider the two asymptotic regimes of a rapid stretching disk $\sigma \gg 1$ and a rapidly shrinking disk $-\sigma \gg 1$.

1. The rapidly stretching disk: $\sigma \gg 1$

The velocity profiles in Fig. 3 for $\sigma > 0$ suggests for large positive σ there exists a boundary layer close to the disk. The thickness of this boundary layer is $O(\sigma^{1/2})$; outside this layer the outer solution is trivially

$$g(z) = 1, \quad f(z) = f_\infty. \tag{A1}$$

The inner solution is found by introducing a new stretched boundary layer variable Z, such that $z = |\sigma|^{1/2} Z$, and the scaled inner functions $F(Z)$ and $G(Z)$,

$$f = \sigma^{1/2} F(Z), \quad g = G(Z). \tag{A2}$$

Introducing these scaled variables into (2.4) leads to

$$F_{ZZZ} + 2FF_{ZZ} - F_Z^2 + \sigma^{-2}(G^2 - 1) = 0, \quad F(0) = 0, \quad F_Z(0) = 1, \quad F_Z(\infty) = 0, \tag{A3a}$$

$$G_{ZZ} + 2(FG_Z - F_Z G) = 0, \quad G(0) = 0, \quad G(\infty) = 1. \tag{A3b}$$

We seek an asymptotic solution to these equations where we expand $F(Z)$ and $G(Z)$ in powers of σ^{-2},

$$F(Z) = F_0(Z) + \sigma^{-2} F_2(Z) + \sigma^{-4} F_4(Z) + O(\sigma^{-6}),$$
$$G(Z) = G_0(Z) + \sigma^{-2} G_2(Z) + \sigma^{-4} G_4(Z) + O(\sigma^{-6}).$$

Inserting these expansions into (3.8) and equating powers of σ^{-2} leads to the following hierarchy of system equations: At $O(1)$,

$$F_{0ZZZ} + 2F_0 F_{0ZZ} - F_{0Z}^2 = 0, \quad F_0(0) = 0, \quad F_{0Z}(0) = 1, \quad F_{0Z}(\infty) = 0,$$
$$G_{0ZZ} + 2(F_0 G_{0Z} - F_{0Z} G_0) = 0, \quad G_0(0) = 0, \quad G_0(\infty) = 1;$$

then at $O(\sigma^{-2})$,

$$F_{2ZZZ} + 2(F_0 F_{2ZZ} + F_2 F_{0ZZ}) - 2F_{0Z} F_{2Z} + G_0^2 - 1 = 0, \quad F_2(0) = 0, \quad F_{2Z}(0) = 0, \quad F_{2Z}(\infty) = 0,$$
$$G_{2ZZ} + 2(F_0 G_{2Z} + F_2 G_{0Z} - F_{0Z} G_2 - F_{2Z} G_0) = 0, \quad G_2(0) = 0, \quad G_2(\infty) = 0;$$

and at $O(\sigma^{-4})$,

$$F_{4ZZZ} + 2(F_0 F_{4ZZ} + F_2 F_{2ZZ} + F_4 F_{0ZZ}) - 2F_{0Z} F_{4Z} - F_{2Z}^2 + 2G_0 G_2 = 0,$$
$$F_4(0) = 0, \quad F_{4Z}(0) = 0, \quad F_{4Z}(\infty) = 0,$$
$$G_{4ZZ} + 2(F_0 G_{4Z} + F_2 G_{2Z} + F_4 G_{0Z} - F_{0Z} G_4 - F_{2Z} G_2 - F_{4Z} G_0) = 0,$$
$$G_4(0) = 0, \quad G_4(\infty) = 0.$$

These systems of equations are solved consecutively using the same numerical scheme as for the full system. The resulting asymptotic shear stress values are found to be

$$F_{0ZZ}(0) = -1.173\,720\,738\,913, \quad G_{0Z}(0) = 0.528\,652\,929\,118,$$
$$F_{2ZZ}(0) = -0.772\,897\,415\,441, \quad G_{2Z}(0) = 0.203\,722\,589\,589,$$
$$F_{4ZZ}(0) = 0.114\,592\,927\,248, \quad G_{4Z}(0) = -0.071\,141\,123\,212.$$

2. The rapidly shrinking disk: $-\sigma \gg 1$

For $\sigma < 0$ the boundary layer thickness is again $O(|\sigma|^{1/2})$ and the outer solution is also (A1). Using the same boundary layer variable Z as in Appendix A 1 but the scaled inner functions $\tilde{F}(Z)$ and $\tilde{G}(Z)$,

$$f = |\sigma|^{1/2}\tilde{F}(Z), \quad g = |\sigma|\tilde{G}(Z),$$

in (2.4) leads to the system

$$\tilde{F}_{ZZZ} + 2\tilde{F}\tilde{F}_{ZZ} - \tilde{F}_Z^2 + \tilde{G}^2 - |\sigma|^{-2} = 0, \quad \tilde{F}(0) = 0, \quad \tilde{F}_Z(0) = -1, \quad \tilde{F}_Z(\infty) = 0, \tag{A4a}$$

$$\tilde{G}_{ZZ} + 2(\tilde{F}\tilde{G}_Z - \tilde{F}_Z\tilde{G}) = 0, \quad \tilde{G}(0) = 0, \quad \tilde{G}(\infty) = |\sigma|^{-1}. \tag{A4b}$$

The $|\sigma|^{-1}$ term in the boundary condition for $\tilde{G}$ suggests an asymptotic solution in the form

$$\tilde{F}(Z) = \tilde{F}_0(Z) + |\sigma|^{-1}\tilde{F}_1(Z) + |\sigma|^{-2}\tilde{F}_2(Z) + O(|\sigma|^{-3}),$$
$$\tilde{G}(Z) = \tilde{G}_0(Z) + |\sigma|^{-1}\tilde{G}_1(Z) + |\sigma|^{-2}\tilde{G}_2(Z) + O(|\sigma|^{-3}).$$

Inserting these expansions into (3.10) and equating powers of $|\sigma|^{-1}$ leads to the following hierarchy of system equations: At $O(1)$,

$$\tilde{F}_{0ZZZ} + 2\tilde{F}_0\tilde{F}_{0ZZ} - \tilde{F}_{0Z}^2 + \tilde{G}_0^2 = 0 \quad \tilde{F}_0(0) = 0, \quad \tilde{F}_{0Z}(0) = -1, \quad \tilde{F}_{0Z}(\infty) = 0,$$
$$\tilde{G}_{0ZZ} + 2(\tilde{F}_0\tilde{G}_{0Z} - \tilde{F}_{0Z}\tilde{G}_0) = 0 \quad \tilde{G}_0(0) = 0, \quad \tilde{G}_0(\infty) = 0;$$

then at $O(|\sigma|^{-1})$,

$$\tilde{F}_{1ZZZ} + 2(\tilde{F}_0\tilde{F}_{1ZZ} + \tilde{F}_1\tilde{F}_{0ZZ}) - 2\tilde{F}_{0Z}\tilde{F}_{1Z} + 2\tilde{G}_0\tilde{G}_1 = 0, \ \tilde{F}_1(0) = 0, \ \tilde{F}_{1Z}(0) = 0, \ \tilde{F}_{1Z}(\infty) = 0,$$
$$\tilde{G}_{1ZZ} + 2(\tilde{F}_0\tilde{G}_{1Z} + \tilde{F}_1\tilde{G}_{0Z} - \tilde{F}_{0Z}\tilde{G}_1 - \tilde{F}_{1Z}\tilde{G}_0) = 0, \ \tilde{G}_1(0) = 0, \ \tilde{G}_1(\infty) = 1;$$

and at $O(|\sigma|^{-2})$,

$$\tilde{F}_{2ZZZ} + 2(\tilde{F}_0\tilde{F}_{2ZZ} + \tilde{F}_1\tilde{F}_{1ZZ} + \tilde{F}_2\tilde{F}_{0ZZ}) - 2\tilde{F}_{0Z}\tilde{F}_{2Z} - \tilde{F}_{1Z}^2 + 2\tilde{G}_0\tilde{G}_2 + \tilde{G}_1^2 - 1 = 0,$$
$$\tilde{F}_2(0) = 0, \quad \tilde{F}_{2Z}(0) = 0, \quad \tilde{F}_{2Z}(\infty) = 0,$$
$$\tilde{G}_{2ZZ} + 2(\tilde{F}_0\tilde{G}_{2Z} + \tilde{F}_1\tilde{G}_{1Z} + \tilde{F}_2\tilde{G}_{0Z} - \tilde{F}_{0Z}\tilde{G}_2 - \tilde{F}_{1Z}\tilde{G}_1 - \tilde{F}_{2Z}\tilde{G}_0) = 0,$$
$$\tilde{G}_2(0) = 0, \quad \tilde{G}_2(\infty) = 0.$$

Numerically solving these systems give the asymptotic shear stress values as

$$\tilde{F}_{0ZZ}(0) = -0.725\,131\,902\,079, \quad \tilde{G}_{0Z}(0) = 1.157\,973\,962\,096,$$
$$\tilde{F}_{1ZZ}(0) = -0.000\,000\,000\,088, \quad \tilde{G}_{1Z}(0) = 0.000\,000\,000\,018,$$
$$\tilde{F}_{2ZZ}(0) = -0.633\,741\,006\,320, \quad \tilde{G}_{2Z}(0) = 0.690\,472\,088\,227.$$

APPENDIX B: COEFFICIENTS OF THE LARGE-z ASYMPTOTIC EXPANSION

In the large-z asymptotic form of $g(z)$ in (3.7) the coefficients α, β, and γ are given by

$$\alpha = \frac{\zeta_1 + \zeta_2}{8\left(8f_\infty\lambda_r^3 + 4\lambda_r^4 + 4f_\infty^2\lambda_r^2 + 1\right)},$$
$$\beta = \frac{1}{8\left(\pi_1^2 + \pi_2^2\right)}[\pi_1(\zeta_1 - \zeta_2) + \pi_2\zeta_3],$$
$$\gamma = \frac{1}{8\left(\pi_1^2 + \pi_2^2\right)}[-\pi_2(\zeta_1 - \zeta_2) + \pi_1\zeta_3],$$

where

$$
\begin{aligned}
\pi_1 &= 8f_\infty\lambda_r^3 - 24f_\infty\lambda_i^2\lambda_r + 4\lambda_i^4 - 24\lambda_i^2\lambda_r^2 + 4\lambda_r^4 - 4f_\infty^2\lambda_i^2 + 4f_\infty^2\lambda_r^2 + 1,\\
\pi_2 &= -8\lambda_i(f_\infty + 2\lambda_r)\big(f_\infty\lambda_r - \lambda_i^2 + \lambda_r^2\big),\\
\zeta_1 &= \tfrac{1}{2}\big(8f_\infty^2\lambda_i^2 - 4f_\infty^2\lambda_r^2 + 4f_\infty\lambda_i^2\lambda_r - 4f_\infty\lambda_r^3 + \lambda_i^4 - 4\lambda_i^2\lambda_r^2 - \lambda_r^4 - 4\big)A^2\\
&\quad - \lambda_i^2\big(4f_\infty\lambda_r - \lambda_i^2 + 5\lambda_r^2 - 2f_\infty^2\big)B^2\\
&\quad - 2\lambda_i(f_\infty + \lambda_r)\big(2f_\infty\lambda_r - \lambda_i^2 + \lambda_r^2\big)AB,\\
\zeta_2 &= -\lambda_i^2\big(4f_\infty\lambda_r - \lambda_i^2 + 5\lambda_r^2 - 2f_\infty^2\big)A^2\\
&\quad + \tfrac{1}{2}\big(8f_\infty^2\lambda_i^2 - 4f_\infty^2\lambda_r^2 + 4f_\infty\lambda_i^2\lambda_r - 4f_\infty\lambda_r^3 + \lambda_i^4 - 4\lambda_i^2\lambda_r^2 - \lambda_r^4 - 4\big)B^2\\
&\quad + 2\lambda_i(f_\infty + \lambda_r)\big(2f_\infty\lambda_r - \lambda_i^2 + \lambda_r^2\big)AB,\\
\zeta_3 &= 2\lambda_i(f_\infty + \lambda_r)\big(2f_\infty\lambda_r - \lambda_i^2 + \lambda_r^2\big)(A^2 - B^2)\\
&\quad + \big(4f_\infty^2\lambda_i^2 - 4f_\infty^2\lambda_r^2 + 12f_\infty\lambda_i^2\lambda_r - 4f_\infty\lambda_r^3 - \lambda_i^4 + 6\lambda_i^2\lambda_r^2 - \lambda_r^4 - 4\big)AB.
\end{aligned}
$$

[1] U. T. Bödewadt, Die drehströmung über festem grunde, Z. Angew Math. Mech. **20**, 241 (1940).
[2] M. Itoh, Y. Yamada, S. Imao, and M. Gonda, in *Proceedings of the First Symposium on Measurements Engineering Turbulence Modelling*, edited by W. Rodi and E. C. Canic (Elsevier, New York, 1990), pp. 659–668.
[3] J. M. Owen, Air-cooled gas turbine discs: A review of recent research, Int. J. Heat and Fluid Flow **9**, 354 (1988).
[4] T. von Kármán, Über laminare und turbulente reibung, Z. Angew Math. Mech. **1**, 233 (1921).
[5] V. W. Ekman, On the influence of the earth's rotation on ocean currents, Ark. Mat. Astron. Fys. **2**, 1 (1905).
[6] Ö. Savaş, Circular waves on stationary disk in rotating flow, Phys. Fluids. **26**, 3445 (1983).
[7] Ö. Savaş, Stability of Bödewadt flow, J. Fluid Mech. **183**, 77 (1987).
[8] J. M. Lopez and P. D. Weidman, Stability of stationary endwall boundary layers during spin-down, J. Fluid Mech. **326**, 373 (1996).
[9] R. Fernandez-Feria, Axisymmetric instabilities of Bödewadt flow, Phys. Fluids **12**, 1730 (2002).
[10] S. O. Mackerrell, Stability of Bödewadt flow, Philos. Trans. R. Soc. A **363**, 1181 (2005).
[11] R. J. Lingwood, Absolute instability of the boundary layer on a rotating disk, J. Fluid Mech. **299**, 17 (1995).
[12] R. J. Lingwood, Absolute instability of the Ekman layer and related rotating flows, J. Fluid Mech. **331**, 405 (1997).
[13] P. Huerre and P. A. Monkewitz, Local and global instabilities in spatially developing flows, Annu. Rev. Fluid Mech. **22**, 473 (1990).
[14] R. J. Briggs, *Electron-Stream Interaction with Plasmas* (MIT Press, Cambridge, 1964).
[15] P. J. Schmid and D. S. Henningson, *Stability and Transition in Shear Flows* (Springer, New York, 2001).
[16] J. J. Healey, Long-wave theory for the absolute instability of the rotating-disc boundary layer, Proc. R. Soc. A **462**, 1467 (2006).
[17] W. H. Press, B. P. Flannery, S. A. Teukolsky, and W. T. Vetterling, *Numerical Recipes (FORTRAN version)* (Cambridge University Press, Cambridge, 1989).
[18] B. Sahoo, S. Abbasbandy, and S. Poncet, A brief note on the computation of the Bödewadt flow with Navier slip boundary conditions, Comput. Fluids **90**, 133 (2014).
[19] L. Brevdo and T. J. Bridges, Absolute and convective instabilities of spatially periodic flows, Philos. Trans. R. Soc. A **354**, 1027 (1996).

[20] J. J. Healey, Enhancing the absolute instability of a boundary layer by adding a far-away plate, J. Fluid Mech. **579**, 29 (2007).
[21] M. P. Juniper, The full impulse response of two-dimensional jet/wake flows and implications for confinement, J. Fluid Mech. **590**, 163 (2007).
[22] M. R. Turner, J. J. Healey, S. S. Sazhin, and R. Piazzesi, Stability analysis and break-up length calculations for steady planar liquid jets, J. Fluid Mech. **668**, 384 (2011).
[23] D. J. Benney and R. F. Bergeron, A new class of nonlinear waves in parallel flows, Stud. Appl. Math. **48**, 181 (1969).